

Laser threshold magnetometer reaching attotesla precision

Jan Jeske, Jared H. Cole, and Andrew D. Greentree

Chemical and Quantum Physics, School of Applied Sciences, RMIT University, Melbourne 3001, Australia

We propose a new type of sensor, which uses diamond containing the optically active nitrogen-vacancy (NV) centres as a laser medium. The magnetometer can be operated at room-temperature and generates light that can be readily fibre coupled, thereby permitting use in industrial applications and remote sensing. By combining laser pumping with a radio-frequency Rabi-drive field, an external magnetic field changes the fluorescence of the NV centres. We use this change in fluorescence level to push the laser above threshold, turning it on with an intensity controlled by the external magnetic field, which provides a coherent amplification of the readout signal with very high contrast. This provides the advantage over conventional NV-based magnetometers which use fluorescence measurements, based on incoherent photon emission, and are currently experimentally limited to few nT/ $\sqrt{\text{Hz}}$. By contrast we predict that an NV-based laser threshold magnetometer with a volume of 1mm^3 can achieve shot-noise limited d.c. sensitivity of $1.42\text{ aT}/\sqrt{\text{Hz}}$ and a.c. sensitivity of $2.34\text{ aT}/\sqrt{\text{Hz}}$. We term our approach laser threshold magnetometry (LTM).

The precise measurement of magnetic fields (magnetometry) has a variety of scientific applications including NMR detection and gravitational wave detection. More generally, it is an enabling technology for mining exploration, to detect oil, gas and mineral reserves[1, 2], in airports for automated detection of plane movements with less building-induced interference than radar[3, 4], and in medicine for the detection of magnetic fields produced by the heart (magneto-cardiography - MCG) or brain (magneto-encephalography - MEG)[5–8]. New room-temperature operated sensors with better sensitivities would enable new mapping techniques at higher spatial resolution. Current state-of-the-art sensors with sensitivities around $1\text{ fT}/\sqrt{\text{Hz}}$ are the widely used SQUID magnetometers[9, 10], operated at cryogenic temperatures below 10 K, and the more recent spin-exchange relaxation-free (SERF) atomic magnetometers [11]. Diamond containing negatively-charged nitrogen-vacancy (NV) centres has emerged as being important for niche applications including room-temperature nanoscale magnetometry [12–15]. Our calculations assume that all of the NV centres are oriented parallel to each other, and we note that preferentially aligned NV centres can be achieved [16]. Small populations in non-optimal orientations do not affect our results significantly.

The NV colour centre in diamond possesses numerous outstanding properties, that have made it ideal for quantum applications. In particular, because of efficient optical spin polarisation and readout [17], it has been identified as a biocompatible nanoscale magnetometer [13–15, 18], electrometer [19, 20], thermometer[21–23] and quantum environment sensor [24–26]. For a comprehensive description of the NV centre, see Doherty *et al.* [27].

Much of the work on NV sensing has concentrated on the use of single centres, so as to achieve the smallest volume possible, however there have also been investigations of NV ensemble-based magnetometry [28–32]. Whilst such approaches provide improved signal to noise over single centres by increasing the number

of atoms, such improvements are not predicted to give more than a \sqrt{N} improvement, where N is the total number of centres capable of sensing. In current experiments NV-magnetometry based on fluorescence measurements is typically limited to few nT/ $\sqrt{\text{Hz}}$ [32–34].

Here we propose an alternative mechanism for magnetometry, illustrated in Fig. 1(a). Crucially, instead of direct fluorescence measurements of NV ensembles, a laser is constructed from the NV centres themselves. The central idea is to use the change in fluorescence that arises because of the magnetic-field dependent spin populations, to shift the laser from below threshold to above threshold Fig. 1(b). This gives rise to a coherent output signal from the NV ensemble, indicative of the magnetic field strength, with a twofold advantage. The laser signal strength can vary by many orders of magnitude, greatly improving contrast, while direct fluorescence measurements require the discrimination between two relatively similar intensities (typically a 20% difference in fluorescence levels for single NV centres [15]). Furthermore, stimulated emission amplifies the rate of emitted photons and puts them into the same spatial mode, ideally permitting the collection of all emitted photons. In contrast, the collection efficiency of conventional NV magnetometry is limited by the numerical aperture of the optics used to image the NV, which emit into all space. Laser threshold magnetometry (LTM) leads to milliwatt photon power output and a commensurate increase in sensitivity to the aT/ $\sqrt{\text{Hz}}$ scale.

While diamond is used as a laser medium for Raman lasers [35], and diamond UV LEDs have also been demonstrated [36], we are unaware of any diamond-based magnetometer with the sensitivities we predict here. LTM will lead to magnetometers with sensitivities 9 orders of magnitude better than existing NV demonstrations and 2-3 orders of magnitude better than state-of-the art SQUID and SERF magnetometers.

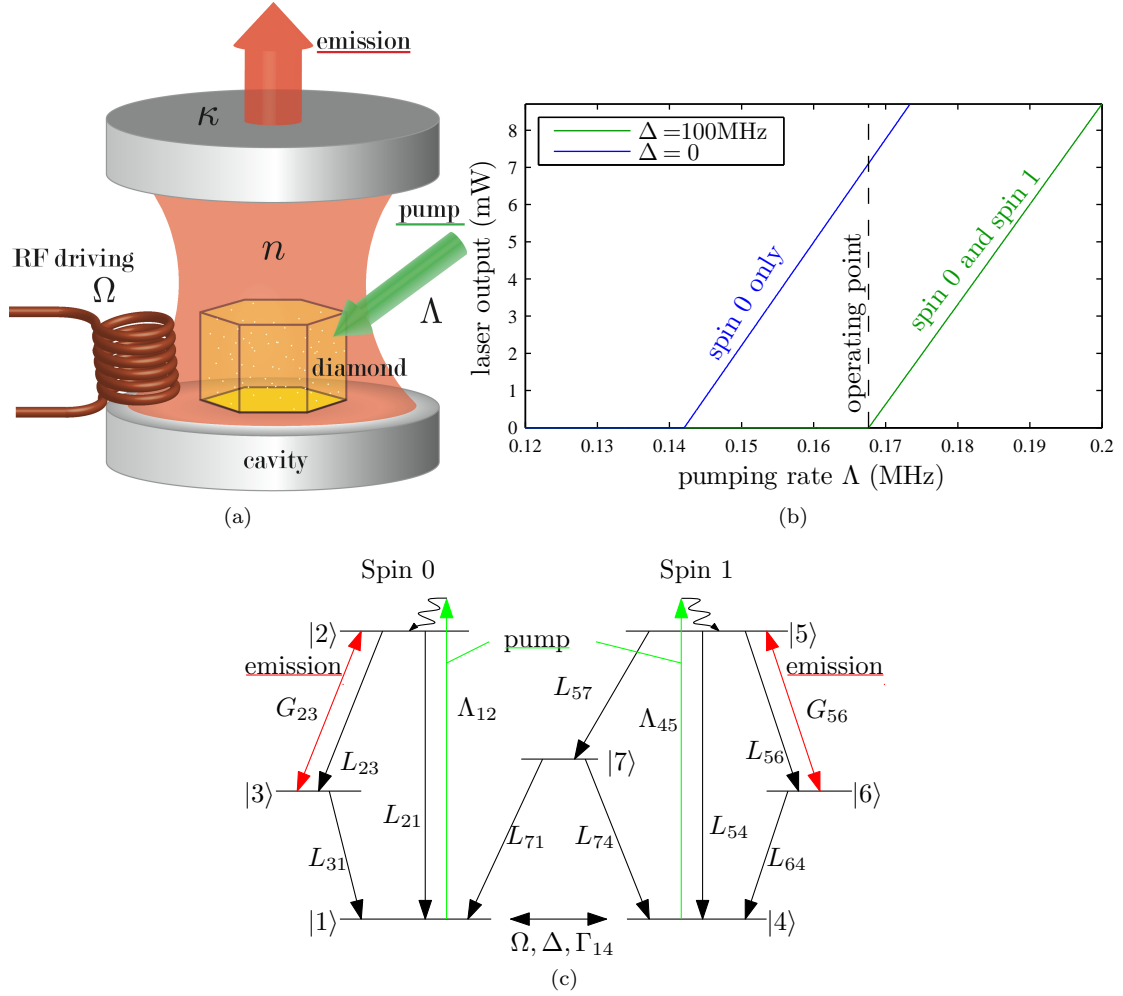


FIG. 1: (A) Concept for a nitrogen-vacancy (NV) laser system using laser threshold magnetometry (LTM). NV is the laser gain medium, pumped in the green and lasing on the red three phonon sideband. (b) The laser output over the pumping rate when the RF drive is off-resonant, $\Delta = 100\text{MHz}$, or on-resonant, $\Delta = 0$. The lasing threshold is dependent on the spin manifold. The operating point is chosen in between such that the laser turns on and off depending on the magnetic resonance of the spin manifolds and achieves maximal sensitivity. Setting the operating point to $\Lambda = 0.168\text{ MHz}$ ensures the laser turns off at $\Delta = 0$ and maximises the laser output at $\Delta = 100\text{ MHz}$. The Rabi frequency is $\Omega = 5\text{ MHz}$. (c) Reduced level structure for NV, breaking the system into the manifolds for spin 0 and spin 1 and highlighting the state transitions. Mixing between the manifolds is only possible via the singlet pathway, which takes population from the spin 1 manifold to the spin 0 manifold, and via the RF drive, which in the incoherent limit tends to equalise populations. The green pump laser lifts population into a phonon-added state just above $|2\rangle$ and $|5\rangle$, followed by a very rapid decay into $|2\rangle, |5\rangle$. The $|2\rangle \leftrightarrow |3\rangle$ and $|5\rangle \leftrightarrow |6\rangle$ transitions emit into the cavity.

RESULTS

A nitrogen-vacancy laser

The electronic ground state manifold of the NV centre is a spin one triplet, which at zero magnetic field has a spin-0 ground state, and nearly-degenerate spin ± 1 states at 2.88 GHz , due to the crystal field splitting [37]. For our purposes we will treat it as a spin half system, assuming that optical pumping into the spin 0 ground state is

perfect [38], and the radio-frequency (RF) field that induces spin flips is only resonant with one of the ± 1 spin states. We further assume that all of the processes except for the singlet pathway and the RF drive field are spin conserving. Hence we can separate the problem into two manifolds, the spin 0 manifold and the spin 1 manifold. A schematic of the pertinent energy levels of the NV system is given in Fig. 1(c). The 3A_2 spin 0 and spin 1 states are denoted by $|1\rangle$ and $|4\rangle$ respectively and have a energy difference that changes linearly with ex-

ternal magnetic field. An external RF drive can induce coherent Rabi oscillations at frequency Ω and detuning Δ between these two states, i.e. Δ also changes linearly with external magnetic field. Γ_{14} is the ground-state decoherence. A green pump laser drives population to a phonon-added state just above the 3E spin 0 and spin 1 states, denoted by $|2\rangle$ and $|5\rangle$ respectively, followed by a rapid decay into $|2\rangle, |5\rangle$. This effectively incoherent driving is spin-conserving: $|1\rangle \rightarrow |2\rangle$ and $|4\rangle \rightarrow |5\rangle$. The system decays from $|2\rangle, |5\rangle$ via several decay paths back to states $|1\rangle$ and $|4\rangle$: Direct decay creating a photon, indirect decay creating a photon of less energy and one or more phonons - the phonon sidebands, and decay via the singlet states 1A_1 and 1E , for simplicity represented by only one state $|7\rangle$. Due to this relatively long-lived singlet pathway a spin polarisation mechanism occurs such that spin 1 population is more likely to be pumped to spin 0. Because the singlet pathway is longer lived than the direct emission, the spin 0 state is slightly brighter than the spin 1 state. This mechanism is used elsewhere for both spin polarisation and readout of an individual NV centre. We use the difference in fluorescence to shift the laser threshold based on external magnetic fields.

As the branching ratio to the 3 phonon sideband is the strongest [27, 39, 40], we denote the 3 phonon added ground state in the respective spin manifold by states $|3\rangle, |6\rangle$ and consider lasing on the $|2\rangle \leftrightarrow |3\rangle$ and $|5\rangle \leftrightarrow |6\rangle$ transition while all other sidebands are included into one effective direct decay. The phononic states $|3\rangle, |6\rangle$ are only virtual levels and relax very rapidly via phononic processes to the ground states, $|1\rangle, |4\rangle$. Hence for our purposes we require population inversion between $|3\rangle$ and $|2\rangle$ or between $|6\rangle$ and $|5\rangle$ respectively. The L_{ij} represent incoherent decay rates within the NV centre and the G_{ij} the coherent (cavity induced) transitions, $\Lambda_{12}, \Lambda_{45}$ represent effectively incoherent pumping rates from the green laser pump. Finally n is the number of intracavity photons per NV centre and κ is the photonic loss rate from the cavity, which determine the red laser output power P_{out} :

$$P_{out} = 2\pi n N_{at} \kappa \hbar \nu_{23} \quad (1)$$

where N_{at} is the number of NV centres in the cavity. The laser output power and pumping power both scale linearly with κ in the relevant parameter regime (input via linear dependence on the operating point). This means laser pump power is another tunable parameter although in practice the output will be limited by the input power one can provide to the diamond crystal.

Realistic parameters

For simplicity and due to lack of separate experimental data on each spin manifold, we will assume the cavity-induced transitions $G_{23} = G_{56} = G$ and all correspond-

ing rates in the two spin manifolds to be the same $L_{23} = L_{56}, L_{31} = L_{64}$ and $L_{21} = L_{54}$. The only exceptions are $L_{74} = (462\text{ns})^{-1}$, $L_{71} = L_{74}/2$ and $L_{57} = (24.9\text{ns})^{-1}$, based on ref. [27], which define a non-spin-conserving decay path. The cavity-induced transitions G describe the stimulated emission and absorption rates and are dependent on the cavity volume V_c , and N_{at} [41, 42]

$$G = 3\nu_{23} L_{23} \lambda^3 N_{at} / (4\pi^2 \Delta \nu_{23} V_c) \quad (2)$$

with the transition frequency $\nu_{23} = c/709\text{nm}$ (1.75eV photon energy, see fig. 11 in [27]), the corresponding wavelength $\lambda = 709\text{nm}/2.4$, where 2.4 is the refractive index of diamond, the peak width of the three phonon sideband $\Delta \nu_{23} \approx 24\text{THz}$, [43]. Assuming a density of NV centres of 1 per $(100\text{nm})^3$, which corresponds to 5.7 ppb, and both a laser medium volume and cavity volume of $V_c = 1\text{mm}^3$ we find a cavity-induced transition rate of $G_{23} = G_{56} = G = 585\text{MHz}$. The spontaneous decay rate to the three-phonon sideband is $L_{23} = L_{56} = 18\text{MHz}$ and the direct decay rate $L_{21} = L_{54} = 68.2\text{MHz}$ [44, 45]. The phononic decay is much faster and set to $L_{31} = L_{64} = 1\text{THz}$, since the exact value is unknown, but unimportant as it is fast compared to the other decay rates, and small compared with the transition frequencies. The dephasing rate is set to $\Gamma_{14} = (6\mu\text{s})^{-1}$ which is a conservative estimate for ensembles of NV centres [27]. The cavity loss rate is set to an easily achievable $\kappa = 1\text{MHz}$, which corresponds to a cavity $Q = 2\pi\nu_{23}/\kappa = 2.7 \times 10^9$, neglecting all other losses. This cavity design is large compared to those used in semiconductor laser diodes, but compatible with the dimensions of readily available synthetic diamond crystals.

Laser threshold magnetometry

Figure 1(c) shows the laser output power as a function of the laser pumping rate $\Lambda_{12} = \Lambda_{45} = \Lambda$ with resonant ($\Delta = 0$) and off-resonant ($\Delta = 100\text{MHz}$) RF drive. At off-resonant driving, the singlet pathway L_{71} guarantees population to only be in the spin 0 manifold. At resonance, the RF drive mixes the populations of $|1\rangle$ and $|4\rangle$ and works against the singlet pathway, which has a long life-time relative to the triplet emission rates. At resonant driving, the singlet pathway behaves like an additional loss channel of the laser medium, which increases the lasing threshold. In other words, on resonance the population inversion between states $|5\rangle$ and $|6\rangle$ is harder to achieve than the off-resonance population inversion between $|3\rangle$ and $|2\rangle$.

To operate as a high precision magnetometer we choose an operating point such that, on resonance (with population shared amongst the spin 0 and spin 1 manifold) the population is just below threshold, whereas off-resonance (when the system has been optically pumped into the

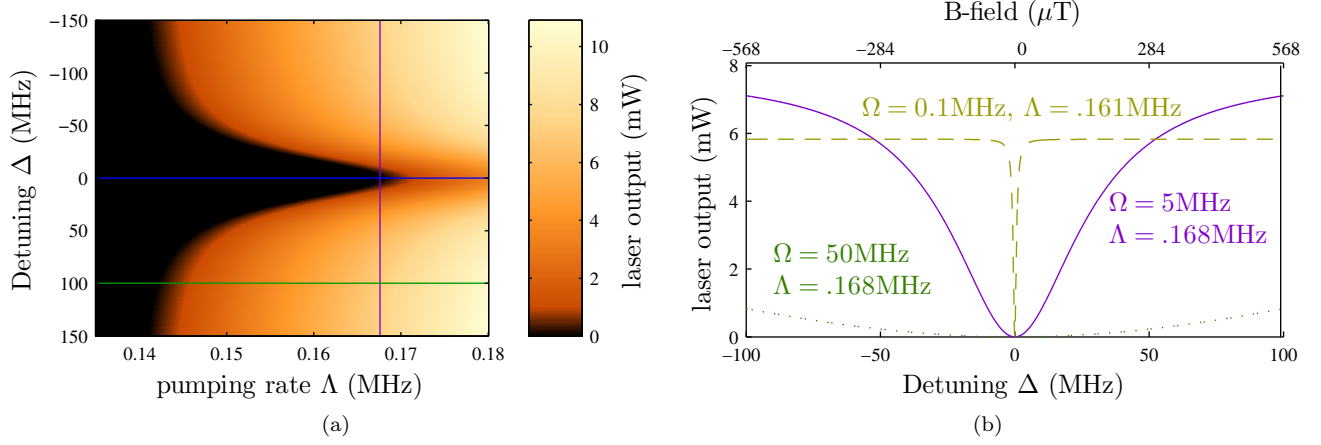


FIG. 2: (a) Laser output power as a function of detuning and pumping rate. The blue and green horizontal lines correspond to the laser thresholds shown in 1(b) for the spin 0 and spin 0+1 cases respectively. The operating point of the pumping rate is ideally set to $\Lambda = 0.168$ MHz (purple line) (b) Laser output power as a function of detuning at the respective operating points. The detuning (bottom axis) and B-field (top axis) can be inferred from the laser output. The purple line (solid) corresponds exactly to the vertical line in (a). One can tune to higher precision (dashed) or greater measurement range (dotted) as required without changing the fabrication parameters: κ , NV density and coherence time. In this plot we have chosen $\kappa = 1$ MHz, $[\text{NV}] = 5.7 \text{ ppb}$, and $T_2 = 6 \mu\text{s}$.

spin 0 ground state) the system is above threshold. This operating range is around $\Lambda = 0.16 \text{ MHz}$ in figure 1(b).

Figure 2(a) shows the laser output power P_{out} in mW as a function of Δ and Λ . Once the pumping rate Λ is set to the desired operating point (purple line), nonzero detuning pushes the system over the lasing threshold. The RF drive sets the initial value for Δ , e.g. zero; any further changes to Δ are then caused by changes in the outer magnetic field, i.e. any non-zero external magnetic field turns the laser on, with an intensity indicative of the magnetic field strength. With no detuning bias, the external magnetic field is given by

$$B = \Delta \frac{\hbar}{g_e \mu_B} \quad (3)$$

i.e. $B/\Delta = 5.68 \mu\text{T}/\text{MHz}$, where g_e is the Landé g-factor and μ_B the Bohr magneton. In this way the device is a highly sensitive magnetic field sensor, or magnetometer, with very high contrast.

Figure 2(b) shows how P_{out} changes with Δ at the operating point $\Lambda = 0.168 \text{ MHz}$ (solid line). Selecting different values of the Rabi-frequency Ω and the pumping rate Λ provides either increased dynamical measurement range (dotted) or increased measurement precision (dashed) as it increases the laser output gradient for small B-fields. As both the RF drive and laser pump are externally controlled parameters, these adjustments do not require changes of fabrication parameters but simply represent different operating modes. The precision could furthermore be increased by scanning across the entire dip via a variation of the detuning to obtain one high-precision measurement of the magnetic field.

The device has a response time t_r to sudden changes of the magnetic field which is essentially set by the slowest process out of RF driving Ω , laser pumping rate Λ , cavity decay κ , and effective non-spin conserving transition rate. For the parameters above, the laser pumping rate is the slowest process and sets $t_r \approx 1/\Lambda = 6.0 \mu\text{s}$ (examples in supplementary material). This can be shortened by increasing κ, Λ, Ω such that the non-spin conserving transition rate sets $t_r \approx 1/L_{57} + 1/L_{71} = 0.5 \mu\text{s}$. Since this non-spin conserving transition rate is not precisely known experimentally, the device can also serve as a probe for this parameter.

Sensitivity

The shot-noise-limited sensitivity of the device is defined as $\eta \equiv B_{min} \sqrt{T}$ where B_{min} is the minimum field that can still be detected in the total measurement time T . Since longer measurements in the presence of shot-noise decrease the error as $1/\sqrt{T}$ this factor must be multiplied with B_{min} to achieve a T -independent value. The sensitivity is:

$$\eta_{dc} = \frac{dB}{dn} \sqrt{\frac{n}{N_{at}\kappa}} \quad (4)$$

The sensitivities corresponding to the different tuning parameters of fig.2(b) are $4900 \text{ fT}/\sqrt{\text{Hz}}$ (dotted), $490 \text{ fT}/\sqrt{\text{Hz}}$ (solid) and $13 \text{ fT}/\sqrt{\text{Hz}}$ (dashed).

Ultrahigh precision can be achieved by increasing our conservative estimates for the NV density and their

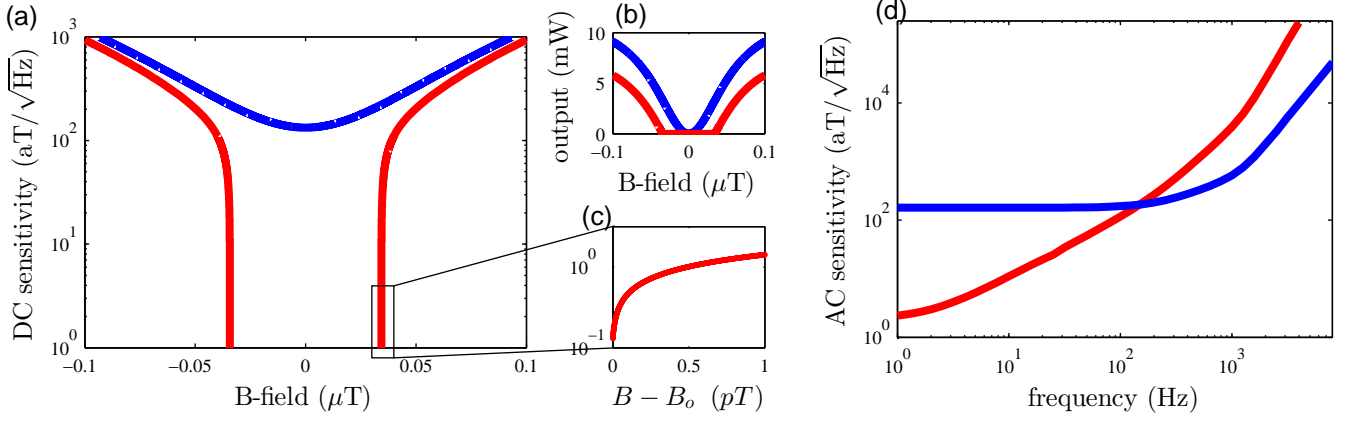


FIG. 3: (a) D.C. Sensitivity as a function of external magnetic field with laser pumping at the operating point $\Lambda = 3.92\text{kHz}$ (blue) and slightly below $\Lambda = 3.8\text{kHz}$ (red). We increased the NV density to 0.57 ppm and the coherence time to $T_2 = 600\mu\text{s}$ and chose $\kappa = 2.5\text{MHz}$, $\Omega = 1.6\text{kHz}$. (b) The laser output for the same parameters as in (a). The red curve has a hard threshold at $\pm 0.034\mu\text{T}$ with a discontinuous gradient due to the lower laser pumping. At this threshold there is a short range of very good sensitivity. (c) In this range, small external magnetic fields of up to 1 pT can be measured with a sensitivity of $1.42\text{aT}/\sqrt{\text{Hz}}$ and below. (d) A.C. Sensitivities as low as $2.34\text{ aT}/\sqrt{\text{Hz}}$ can be reached as a function of the external magnetic a.c. field frequency. Device parameters are the same as in (a). We apply an effective bias d.c. field of $B_o = 0.032\mu\text{T}$ (blue) and $B_o = 0.034\mu\text{T}$ (red) to reach the region where the laser output has the strongest gradient with the external B-field, compare (b).

coherence time by two orders of magnitude each, to 0.57ppm and $T_2 = 600\mu\text{s}$. The coherence time can be prolonged, for example, by using isotopically enriched diamonds and $T_2 = 600\mu\text{s}$ for ensembles of NV have already been measured[27]. These adaptations would enable an optimal sensitivity of $\eta = 0.133\text{ fT}/\sqrt{\text{Hz}}$, i.e. a precision of 0.133fT can be achieved in a 1-second-long measurement. This sensitivity is reached at the centre of the dip and behaves rather smoothly, see blue line in figure 3(a).

The sensitivity can be improved even further by reducing the laser pumping rate Λ slightly such that the laser reaches a hard threshold point as a function of detuning, see red line in figure 3(b). At the threshold point the contrast diverges leading to a sensitivity which goes to zero. However in the detuning range where the laser is off there is no information available, meaning the increased sensitivity is only available in the small range where it starts to diverge, see red line in figure 3(a), i.e. only available for small signals, using a bias magnetic field B_o to the threshold point. For example external fields up to 1pT can be measured in this way with an improved sensitivity of $1.42\text{aT}/\sqrt{\text{Hz}}$, figure 3(c). This is about 9 orders of magnitude better than magnetometry with single NV centres and current experiments with ensembles of NV centres [32, 46], 3 – 5 orders better than the most optimistic projections for ensemble NV magnetometry [14, 46] and about 3 orders better than SQUIDS. However compared to single NV centre magnetometry we have sacrificed the nanometre spatial resolution since our device is about 1mm^3 .

So far we have only considered the measurement of con-

stant (d.c.) magnetic fields. If the sensor is placed in an oscillating (a.c.) magnetic field signal $B(t) = B_S \cos(\omega t)$ then the cavity photon number n and the laser output will vary in phase with the signal. To achieve good response even for very small B-field amplitudes we measure in the presence of an effective d.c. field bias to offset the laser output and maximise the response to external a.c. fields. In the parameters of fig. 3(b) this offset is approximately $0.032\mu\text{T}$ for the thick blue line. For the red line it is $0.034\mu\text{T}$ and offsets the signal just above the lasing threshold into the small region of high sensitivity. The a.c. sensitivity η_{ac} for a laser signal which is caused by an oscillating cavity photon number $n(t) = n_S \cos(\omega t) + n_o$ is calculated as:

$$\eta_{ac} = \frac{dB_S}{dn_S} \sqrt{\frac{n_o I}{N_{at} \kappa}} \quad (5)$$

where the factor $I = 2.43$ stems from the signal's contribution in each oscillation period. The sensitivity as a function of frequency is shown in figure 3(d). The operation mode just above the hard threshold (red line) allows sensitivities down to $2.34\text{ aT}/\sqrt{\text{Hz}}$ for low frequencies and small signal amplitudes (here: $B_S = 1\text{ pT}$). Operating the magnetometer at the threshold driving with an offset (blue line) yields a sensitivity of $0.16\text{ fT}/\sqrt{\text{Hz}}$ for low frequencies and better sensitivities than the red line above 0.1kHz . Sensitivities to frequencies above 10kHz are worse due to the finite response time of the lasing process; for measurements in this frequency region the sensitivity could be improved by parameters which minimize the response time.

DISCUSSION

We have presented the concept of lasing threshold magnetometry (LTM) and shown that with NV centres in diamond as the laser medium a sensitivity of $1.42 \text{ aT}/\sqrt{\text{Hz}}$ can be achieved using a diamond volume of 1 mm^3 with an NV density 0.57 ppm . This sensitivity is about 10^9 times better than magnetometry with single NV centres, and exceeds current state-of-the-art magnetometers such as SQUID and SERF.

The magnetometer can be kept relatively small and the laser output could be guided into an optic fibre, making the sensor very mobile. The device furthermore can be operated at room temperature. This is a significant technological advantage over the standard SQUID sensors, which need to be operated at cryogenic temperatures (below 10 K). This could particularly improve Magnetoencephalography (MEG) [5, 8], which measures the weak 10 fT - 1 pT magnetic fields [5] produced by brain activity with less distortion [8] than electro-encephalography (EEG).

We have chosen NV centres as our laser medium as they have a one-directional non-spin conserving transition and its properties are very well studied. In principle, LTM can be performed with other color centres for example, the silicon-vacancy centre in diamond, which seems particularly promising [47, 48]

METHODS

Equations of motion and steady state solution

We take as our reduced model a seven state system, with the intracavity photon field, shown in Fig.1(a). We also assume that the only non-negligible coherence ρ_{14} is at the ground state transition. The equations of motion for this simplified structure are:

$$\begin{aligned}
 \dot{\rho}_{11} &= 2i\Omega\Im(\rho_{14}) - \Lambda_{12}\rho_{11} + L_{21}\rho_{22} + L_{31}\rho_{33} + L_{71}\rho_{77}, \\
 \dot{\rho}_{14} &= (i\Delta - \Gamma_{14} - \Lambda_{12}/2 - \Lambda_{45}/2)\rho_{14} - i\Omega(\rho_{55} - \rho_{11}), \\
 \dot{\rho}_{22} &= \Lambda_{12}\rho_{11} - (L_{21} + L_{23})\rho_{22} - G_{34}(\rho_{22} - \rho_{33})n, \\
 \dot{\rho}_{33} &= L_{23}\rho_{22} - L_{31}\rho_{33} - G_{23}(\rho_{33} - \rho_{22})n, \\
 \dot{\rho}_{44} &= -2i\Omega\Im(\rho_{14}) - \Lambda_{45}\rho_{44} + L_{54}\rho_{55} + L_{64}\rho_{66} + L_{74}\rho_{77}, \\
 \dot{\rho}_{55} &= \Lambda_{45}\rho_{44} - (L_{54} + L_{56} + L_{57})\rho_{55} - G_{56}(\rho_{55} - \rho_{66})n, \\
 \dot{\rho}_{66} &= L_{56}\rho_{55} - L_{64}\rho_{66} - G_{56}(\rho_{66} - \rho_{55})n, \\
 \dot{\rho}_{77} &= L_{57}\rho_{55} - (L_{71} + L_{74})\rho_{77}, \\
 \dot{n} &= G_{23}(\rho_{22} - \rho_{33})n + G_{56}(\rho_{55} - \rho_{66})n - \kappa n, \quad (6)
 \end{aligned}$$

where the Λ_{ij} represent effectively incoherent pumping rates from the green laser pump, which model the coherent excitation to a phonon-added state just above $|2\rangle$, followed by a rapid decay into $|2\rangle$. The L_{ij} represent incoherent decay rates within the NV centre and the G_{ij}

the coherent (cavity induced) transitions. The strength of the RF drive is given by Ω - the Rabi frequency, which has detuning Δ , whilst Γ_{14} is the ground-state decoherence. The ρ represent the density matrix elements for the atoms (fraction of the population in each state for the on-diagonal elements). Finally n is the number of intracavity photons per NV centre, κ is the photonic loss rate from the cavity and conservation of population implies $\sum_i \rho_{ii} = 1$.

The steady state solution of the equations of motion gives insight into the lasing threshold and laser output of the system and their dependence on the tunable parameters, such as laser pumping rate Λ_{12} , Λ_{56} , Rabi frequency Ω and detuning Δ . We obtain the steady state by diagonalisation of the superoperator for the density matrix and subsequent solution of equation 6, see supplementary material. We have a full analytical solution and inserted the realistic parameters given in the text.

In all calculations we ignored the possibility of a smaller transition rate in the other spin direction, from $|2\rangle$ to $|7\rangle$. An inclusion of this rate at $L_{27} = 0.01L_{57}$ in the calculations yielded no significant changes of the results, particularly regarding the sensitivity.

We acknowledge useful conversations with W. J. Munro, B. Moran and B. C. Gibson. ADG also acknowledges the ARC for financial support (DP130104381).

Appendix

Method for finding the steady state solution of the equations of motion

The equations of motion for our simplified model are:

$$\begin{aligned}
 \dot{\rho}_{11} &= 2i\Omega\Im(\rho_{14}) - \Lambda_{12}\rho_{11} + L_{21}\rho_{22} + L_{31}\rho_{33} + L_{71}\rho_{77}, \\
 \dot{\rho}_{14} &= (i\Delta - \Gamma_{14} - \Lambda_{12}/2 - \Lambda_{45}/2)\rho_{14} - i\Omega(\rho_{55} - \rho_{11}), \\
 \dot{\rho}_{22} &= \Lambda_{12}\rho_{11} - (L_{21} + L_{23})\rho_{22} - G_{34}(\rho_{22} - \rho_{33})n, \\
 \dot{\rho}_{33} &= L_{23}\rho_{22} - L_{31}\rho_{33} - G_{23}(\rho_{33} - \rho_{22})n, \\
 \dot{\rho}_{44} &= -2i\Omega\Im(\rho_{14}) - \Lambda_{45}\rho_{44} + L_{54}\rho_{55} + L_{64}\rho_{66} + L_{74}\rho_{77}, \\
 \dot{\rho}_{55} &= \Lambda_{45}\rho_{44} - (L_{54} + L_{56} + L_{57})\rho_{55} - G_{56}(\rho_{55} - \rho_{66})n, \\
 \dot{\rho}_{66} &= L_{56}\rho_{55} - L_{64}\rho_{66} - G_{56}(\rho_{66} - \rho_{55})n, \\
 \dot{\rho}_{77} &= L_{57}\rho_{55} - (L_{71} + L_{74})\rho_{77}, \\
 \dot{n} &= G_{23}(\rho_{22} - \rho_{33})n + G_{56}(\rho_{55} - \rho_{66})n - \kappa n, \quad (7)
 \end{aligned}$$

They are nonlinear equations since n is multiplied with the density matrix elements. They can therefore not be solved dynamically via diagonalisation of the superoperator. However for the steady state solution we can assume that all variables are constant (except the oscillation of the off-diagonal elements ρ_{14}, ρ_{41} and therefore treat n as a constant, unknown parameter in the equations of motion. We then rewrite these equations in matrix form on the next page. We then find the steady state solution by finding the nullspace. The unnormalized solution for the populations and coherences ρ_{ij} , as a function of n , is also given on the next page.

With this solution for the $\rho_{ij}(n)$ we can then write down the remaining equation for n . To do so we normalise the solution first by dividing the solution by $\sum_{j=1}^7 \rho_{jj}$. We then insert the normalised steady state solutions for the $\rho_{ij}(n)$ into eq. 7. As we are interested in the steady state we set $\dot{n} = 0$ in the equation:

$$0 = G_{23}(\rho_{22} - \rho_{33})n + G_{56}(\rho_{55} - \rho_{66})n - \kappa n \quad (8)$$

Note that this has the solution $n = 0$ because we neglected spontaneous emission in the equation. We are interested in the non-zero solution of the equation:

$$0 = G_{23}(\rho_{22} - \rho_{33}) + G_{56}(\rho_{55} - \rho_{66}) - \kappa \quad (9)$$

This equation has two solutions for n , one of which is purely negative and unphysical. We obtained the other solution, however the expression is rather long and unhelpful to be written down explicitly here. It gives the equilibrium value for n as a function of all system parameters.

Lasing populations plot

Figure 4 shows the steady state populations as a function of the detuning for a laser pumping rate above the

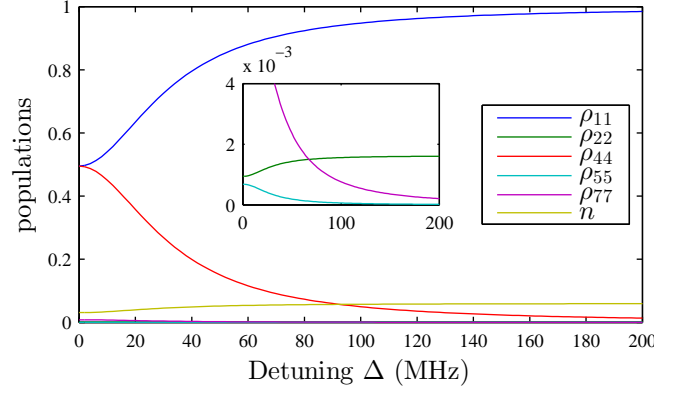


FIG. 4: Populations of the levels in the steady state as a function of detuning Δ for a pumping of $\Lambda = 3\text{MHz}$, that is above both lasing thresholds ($\kappa = 1\text{MHz}$, $\Omega = 5\text{MHz}$). One can see the transition from lasing with populations in spin 0 and spin 1 states (resonant Rabi driving) to lasing with populations only in the spin 0 manifold (off-resonant Rabi driving). The inset shows the curves with very low populations.

operating point, i.e. above the lasing threshold even for large detuning ($n > 0$ in the entire plot). It shows that with increasing detuning, the populations of the spin 1 manifold ($\rho_{44}, \rho_{55}, \rho_{77}$) are reduced to zero; lasing occurs with spin 0 states only and the signal n becomes stronger.

Response time plots

Figure 5 shows numerical simulations of how quickly the device adapts to sudden changes of the magnetic field at $t = 0$ in each plot. In the right column the new equilibrium state is reached after about $100\mu\text{s}$; the parameters correspond to the purple line in figure 2 of the main text. In the left column, parameters were chosen for a faster response time. While the cavity photon number n determines the equilibration of the laser output, the populations of states $|1\rangle$ and $|4\rangle$ give insight into the equilibration process between the spin manifolds. A spontaneous emission rate of 1kHz into the cavity from $|2\rangle$ and $|5\rangle$ was considered in all simulations.

$$\begin{pmatrix} \dot{\rho}_{14} \\ \dot{\rho}_{41} \\ \dot{\rho}_{11} \\ \dot{\rho}_{22} \\ \dot{\rho}_{33} \\ \dot{\rho}_{44} \\ \dot{\rho}_{55} \\ \dot{\rho}_{66} \\ \dot{\rho}_{77} \end{pmatrix} = \begin{pmatrix} \alpha + i\Delta & 0 & i\Omega & 0 & 0 & 0 & -i\Omega & 0 & 0 \\ 0 & \alpha - i\Delta & -i\Omega & 0 & 0 & 0 & i\Omega & 0 & 0 \\ i\Omega & -i\Omega & -\Lambda_{12} & L_{21} & L_{31} & 0 & 0 & 0 & 0 \\ 0 & 0 & \Lambda_{12} & -L_{21} - L_{23} - G_{23}n & G_{23}n & 0 & 0 & 0 & L_{71} \\ 0 & 0 & 0 & L_{23} + G_{23}n & -L_{31} - G_{23}n & 0 & 0 & 0 & 0 \\ -i\Omega & i\Omega & 0 & 0 & 0 & -\Lambda_{45} & L_{54} & L_{64} & L_{74} \\ 0 & 0 & 0 & 0 & 0 & \Lambda_{45} & -L_{54} - L_{56} - L_{57} - G_{56}n & G_{56}n & 0 \\ 0 & 0 & 0 & 0 & 0 & 0 & L_{56} + G_{56}n & -L_{64} - G_{56}n & 0 \\ 0 & 0 & 0 & 0 & 0 & 0 & L_{57} & 0 & -L_{71} - L_{74} \end{pmatrix} \begin{pmatrix} \rho_{14} \\ \rho_{41} \\ \rho_{11} \\ \rho_{22} \\ \rho_{33} \\ \rho_{44} \\ \rho_{55} \\ \rho_{66} \\ \rho_{77} \end{pmatrix}$$

with $\alpha = -\Gamma_{14} - \frac{\Lambda_{12}}{2}$ and $\beta = \Lambda_{12} + \Lambda_{56}$

$$\begin{pmatrix} \frac{iL_{71}(\beta + 2\Gamma_{14} + 2i\Delta)}{2(\beta + 2\Gamma_{14})\Omega} \\ -\frac{iL_{71}(\beta + 2\Gamma_{14} - 2i\Delta)}{2(\beta + 2\Gamma_{14})\Omega} \\ \frac{4(L_{71} + L_{74})(L_{64}(L_{56} + G_{56}n) + L_{54}(L_{64} + G_{56}n))(\beta + 2\Gamma_{14})\Omega^2 + L_{57}(L_{64} + G_{56}n)(4L_{74}(\beta + 2\Gamma_{14})\Omega^2 + L_{71}(\beta^2\Lambda_{45} + 4\beta(\Gamma_{14}\Lambda_{45} + \Omega^2) + 4(\Gamma_{14}^2\Lambda_{45} + \Delta^2\Lambda_{45} + 2\Gamma_{14}\Omega^2)))}{(L_{31} + G_{23}n)\Lambda_{12}(4(L_{71} + L_{74})(L_{64}(L_{56} + G_{56}n) + L_{54}(L_{64} + G_{56}n))(\beta + 2\Gamma_{14})\Omega^2 + L_{57}(L_{64} + G_{56}n)(4L_{74}(\beta + 2\Gamma_{14})\Omega^2 + L_{71}(\beta^2\Lambda_{45} + 4\beta(\Gamma_{14}\Lambda_{45} + \Omega^2) + 4(\Gamma_{14}^2\Lambda_{45} + \Delta^2\Lambda_{45} + 2\Gamma_{14}\Omega^2))))} \\ \frac{4L_{57}(L_{64} + G_{56}n)(L_{31}(L_{23} + G_{23}n) + L_{21}(L_{31} + G_{23}n))(\beta + 2\Gamma_{14})\Omega^2 + L_{71}(\beta^2\Lambda_{45} + 4\beta(\Gamma_{14}\Lambda_{45} + \Omega^2) + 4(\Gamma_{14}^2\Lambda_{45} + \Delta^2\Lambda_{45} + 2\Gamma_{14}\Omega^2))}{(L_{23} + G_{23}n)\Lambda_{12}(4(L_{71} + L_{74})(L_{64}(L_{56} + G_{56}n) + L_{54}(L_{64} + G_{56}n))(\beta + 2\Gamma_{14})\Omega^2 + L_{57}(L_{64} + G_{56}n)(4L_{74}(\beta + 2\Gamma_{14})\Omega^2 + L_{71}(\beta^2\Lambda_{45} + 4\beta(\Gamma_{14}\Lambda_{45} + \Omega^2) + 4(\Gamma_{14}^2\Lambda_{45} + \Delta^2\Lambda_{45} + 2\Gamma_{14}\Omega^2))))} \\ \frac{4L_{57}(L_{64} + G_{56}n)(L_{31}(L_{23} + G_{23}n) + L_{21}(L_{31} + G_{23}n))(\beta + 2\Gamma_{14})\Omega^2 + L_{71}(\beta^2\Lambda_{45} + 4\beta(\Gamma_{14}\Lambda_{45} + \Omega^2) + 4(\Gamma_{14}^2\Lambda_{45} + \Delta^2\Lambda_{45} + 2\Gamma_{14}\Omega^2))}{(L_{71} + L_{74})(L_{56}L_{64} + L_{57}L_{64} + G_{56}L_{57}n + L_{54}(L_{64} + G_{56}n))} \\ \frac{L_{57}(L_{64} + G_{56}n)\Lambda_{45}}{L_{71} + L_{74}} \\ \frac{(L_{71} + L_{74})(L_{56} + G_{56}n)}{L_{57}(L_{64} + G_{56}n)} \\ 1 \end{pmatrix}$$

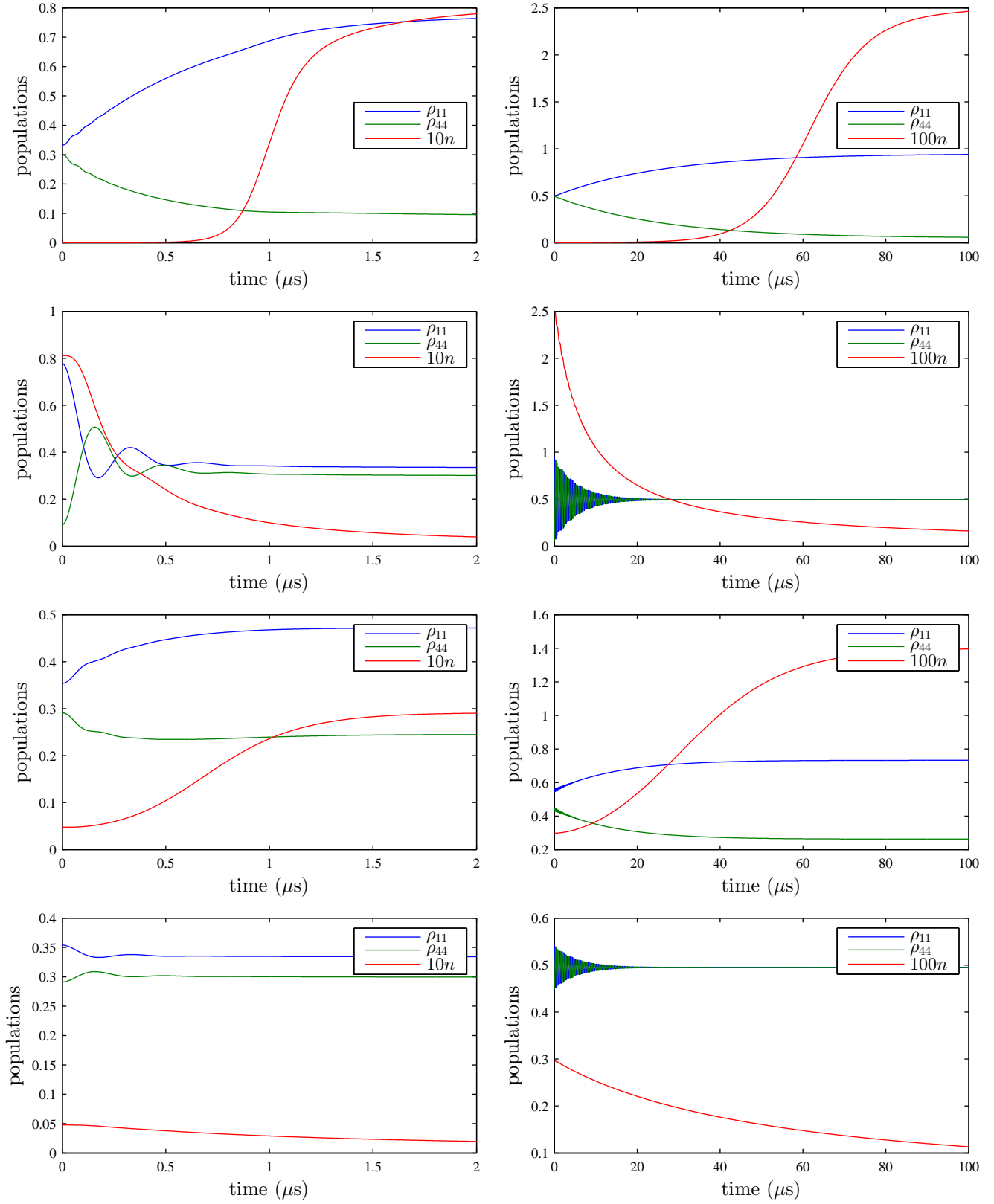


FIG. 5: Time evolution of the state populations and n after an instant change of the detuning Δ . The detuning changes at $t = 0$ from top to bottom: $0 \rightarrow 100\text{MHz}$, $100\text{MHz} \rightarrow 0$, $10\text{MHz} \rightarrow 30\text{MHz}$, $10\text{MHz} \rightarrow 0$. Left: For $\kappa = 40\text{MHz}$, $\Omega = 10\text{MHz}$, $\Lambda = 10.4\text{MHz}$ the device takes about $2\mu\text{s}$ to reach to the new steady state. Right: For the parameters chosen in the main paper, $\kappa = 1\text{MHz}$, $\Omega = 5\text{MHz}$, $\Lambda = 0.168\text{MHz}$ the response time is slower due to a slower laser pumping rate Λ .

-
- [1] M. Nabighian, V. Grauch, R. Hansen, T. LaFehr, Y. Li, J. Peirce, J. Phillips, and M. Ruder, *GEOPHYSICS* **70**, 33 (2005).
- [2] C. P. Foley, K. E. Leslie, R. A. Binks, S. H. K. Lam, J. Du, D. L. Tilbrook, E. E. Mitchell, J. C. Macfarlane, J. B. Lee, R. Turner, M. Downey, and A. Maddever, *Superconductor Science and Technology* **15**, 1641 (2002).
- [3] B. Tamayo, F. Sempere, M. Hernandez, C. Aroca, E. Lopez, M. Sanchez, and P. Sanchez, *Sensors and Actuators A: Physical* **3738**, 442 (1993), proceedings of Eurosensors {VI}.
- [4] C. Stockhammer, H. Gao, T. Heuer, U. Hartmann, K. Dimitropoulos, N. Grammalidis, J. Pfister, and P. Kirrane, in *Intelligent Transportation Systems Conference, 2006. ITSC '06. IEEE* (2006) pp. 510–515.
- [5] M. Hämäläinen, R. Hari, R. J. Ilmoniemi, J. Knuutila, and O. V. Lounasmaa, *Rev. Mod. Phys.* **65**, 413 (1993).
- [6] E. Rodriguez, N. George, J.-P. Lachaux, J. Martinerie, B. Renault, and F. J. Varela, *Nature*, 430 (1999).
- [7] C. D. Gratta, V. Pizzella, F. Tecchio, and G. L. Romani, *Reports on Progress in Physics* **64**, 1759 (2001).
- [8] M. Proudfoot, M. W. Woolrich, A. C. Nobre, and M. R. Turner, *Practical Neurology* **14**, 336 (2014).
- [9] H. Weinstock, *Magnetics, IEEE Transactions on* **27**, 3231 (1991).
- [10] D. Drung, S. Bechstein, K.-P. Franke, M. Scheiner, and T. Schurig, *Applied Superconductivity, IEEE Transactions on* **11**, 880 (2001).
- [11] I. K. Kominis, T. W. Kornack, J. C. Allred, and M. V. Romalis, *Nature*, 596 (2003).
- [12] C. L. Degen, *Applied Physics Letters* **92**, 243111 (2008).
- [13] G. Balasubramanian, I. Y. Chan, R. Kolesov, M. Al-Hmoud, J. Tisler, C. Shin, C. Kim, A. Wojcik, P. R. Hemmer, A. Krueger, T. Hanke, A. Leitenstorfer, R. Bratschitsch, F. Jelezko, and J. Wrachtrup, *Nature* **455**, 648 (2008).
- [14] J. M. Taylor, P. Cappellaro, L. Childress, L. Jiang, D. Budker, P. R. Hemmer, A. Yacoby, R. Walsworth, and M. D. Lukin, *Nature Physics* **4**, 810 (2008).
- [15] J. R. Maze, P. L. Stanwix, J. S. Hodges, S. Hong, J. M. Taylor, P. Cappellaro, L. Jiang, M. V. G. Dutt, E. Togan, A. S. Zibrov, A. Yacoby, R. L. Walsworth, and M. D. Lukin, *Nature* **455**, 644 (2008).
- [16] A. M. Edmonds, U. F. S. D’Haenens-Johansson, R. J. Cruddace, M. E. Newton, K.-M. C. Fu, C. Santori, R. G. Beausoleil, D. J. Twitchen, and M. L. Markham, *Phys. Rev. B* **86**, 035201 (2012).
- [17] F. Jelezko, T. Gaebel, I. Popa, A. Gruber, and J. Wrachtrup, *Physical Review Letters* **92**, 076401 (2004).
- [18] L. P. McGuinness, n. Ya, A. Stacey, D. A. Simpson, L. T. Hall, D. Maclaurin, S. Prawer, P. Mulvaney, J. Wrachtrup, F. Caruso, R. E. Scholten, and L. C. L. Hollenberg, *Nature Nanotechnology* **6**, 358 (2011).
- [19] F. Dolde, H. Fedder, M. W. Doherty, T. Nobauer, F. Rempp, G. Balasubramanian, T. Wolf, F. Reinhard, L. C. L. Hollenberg, F. Jelezko, and J. Wrachtrup, *Nature Physics* **7**, 459 (2011).
- [20] F. Dolde, M. W. Doherty, J. Michl, I. Jakobi, B. Naydenov, S. Pezzagna, J. Meijer, P. Neumann, F. Jelezko, N. B. Manson, and J. Wrachtrup, *Phys. Rev. Lett.* **112**, 097603 (2014).
- [21] P. Neumann, I. Jakobi, F. Dolde, C. Burk, R. Reuter, G. Waldherr, J. Honert, T. Wolf, A. Brunner, J. H. Shim, D. Suter, H. Sumiya, J. Isoya, and J. Wrachtrup, *Nano Letters* **13**, 2738 (2013), pMID: 23721106.
- [22] G. Kucsko, P. C. Maurer, N. Y. Yao, M. Kubo, H. J. Noh, P. K. Lo, H. Park, and M. D. Lukin, *Nature* **500**, 54 (2013).
- [23] T. Plakhotnik, M. W. Doherty, J. H. Cole, R. Chapman, and N. B. Manson, *Nano Letters* **14**, 4989 (2014).
- [24] J. H. Cole and L. C. L. Hollenberg, *Nanotechnology* **20**, 495401 (2009).
- [25] L. T. Hall, J. H. Cole, C. D. Hill, and L. C. L. Hollenberg, *Physical Review Letters* **103**, 220802 (2009).
- [26] S. Kaufmann, D. A. Simpson, L. T. Hall, V. Perunicic, P. Senn, S. Steinert, L. P. McGuinness, B. C. Johnson, T. Ohshima, F. Caruso, J. Wrachtrup, R. E. Scholten, P. Mulvaney, and L. Hollenberg, *Proceedings of the National Academy of Sciences* **110**, 10894 (2013).
- [27] M. W. Doherty, N. B. Manson, P. Delaney, F. Jelezko, J. Wrachtrup, and L. C. Hollenberg, *Physics Reports* **528**, 1 (2013).
- [28] F. T. Charnock and T. A. Kennedy, *Phys. Rev. B* **64**, 041201 (2001).
- [29] V. M. Acosta, E. Bauch, M. P. Ledbetter, C. Santori, K.-M. C. Fu, P. E. Barclay, R. G. Beausoleil, H. Linget, J. F. Roch, F. Treussart, S. Chemerisov, W. Gawlik, and D. Budker, *Phys. Rev. B* **80**, 115202 (2009).
- [30] I. Aharonovich, C. Santori, B. A. Fairchild, J. Orwa, K. Ganesan, K.-M. C. Fu, R. G. Beausoleil, A. D. Greentree, and S. Prawer, *Journal of Applied Physics* **106**, 124904 (2009).
- [31] A. D. Greentree, R. G. Beausoleil, L. C. L. Hollenberg, W. J. Munro, K. Nemoto, S. Prawer, and T. P. Spiller, *New Journal of Physics* **11**, 093005 (2009).
- [32] L. M. Pham, D. L. Sage, P. L. Stanwix, T. K. Yeung, D. Glenn, A. Trifonov, P. Cappellaro, P. R. Hemmer, M. D. Lukin, H. Park, A. Yacoby, and R. L. Walsworth, *New Journal of Physics* **13**, 045021 (2011).
- [33] T. Ishikawa, K.-M. C. Fu, C. Santori, V. M. Acosta, R. G. Beausoleil, H. Watanabe, S. Shikata, and K. M. Itoh, *Nano Letters* **12**, 2083 (2012), pMID: 22404419.
- [34] K. Fang, V. M. Acosta, C. Santori, Z. Huang, K. M. Itoh, H. Watanabe, S. Shikata, and R. G. Beausoleil, *Phys. Rev. Lett.* **110**, 130802 (2013).
- [35] R. P. Mildren and A. Sabella, *Opt. Lett.* **34**, 2811 (2009).
- [36] A. Lohrmann, S. Pezzagna, I. Dobrinets, P. Spinicelli, V. Jacques, J.-F. Roch, J. Meijer, and A. M. Zaitsev, *Applied Physics Letters* **99**, 251106 (2011).
- [37] J. H. N. Loubser and J. A. van Wyk, *Reports on Progress in Physics* **41**, 1201 (1978).
- [38] In practice, the optical pumping into the spin 0 ground state is not perfect, with a flip probability of a few percent. Inclusion of this imperfection did not significantly alter our calculations.
- [39] I. Aharonovich, S. Castelletto, D. A. Simpson, C.-H. Su, A. D. Greentree, and S. Prawer, *Reports on Progress in Physics* **74**, 076501 (2011).
- [40] J. R. Rabeau, S. T. Huntington, A. D. Greentree, and S. Prawer, *Applied Physics Letters* **86**, 134104 (2005).
- [41] A. E. Siegman, *Lasers* (University Science Books, 1986).
- [42] L. M. P. Frank L. Pedrotti, Leno S. Pedrotti, *Introduction to Optics*, third edition ed. (Pearson Prentice Hall, 2007).
- [43] (see figure 22 in [27] or figure 4 in [49]).

- [44] C.-H. Su, *Novel quantum technology based on atom-cavity physics*, Ph.D. thesis, The University of Melbourne (2010).
- [45] C.-H. Su, A. D. Greentree, and L. C. L. Hollenberg, *Opt. Express* **16**, 6240 (2008).
- [46] K. Jensen, N. Leefer, A. Jarmola, Y. Dumeige, V. M. Acosta, P. Kehayias, B. Patton, and D. Budker, *Phys. Rev. Lett.* **112**, 160802 (2014).
- [47] B. Pingault, J. N. Becker, C. H. H. Schulte, C. Arend, C. Hepp, T. Godde, A. I. Tartakovskii, M. Markham, C. Becher, and M. Atature, “All-optical formation of coherent dark states of silicon-vacancy spins in diamond,” arXiv: 1409.4069 (2014).
- [48] L. J. Rogers, K. D. Jahnke, M. H. Metsch, A. Sipahigil, J. M. Binder, T. Teraji, H. Sumiya, J. Isoya, M. D. Lukin, P. Hemmer, and F. Jelezko, “All-optical initialization, readout, and coherent preparation of single silicon-vacancy spins in diamond,” arXiv:1410.1355.
- [49] P. Kehayias, M. W. Doherty, D. English, R. Fischer, A. Jarmola, K. Jensen, N. Leefer, P. Hemmer, N. B. Manson, and D. Budker, *Phys. Rev. B* **88**, 165202 (2013).